Batteries & Supercaps

Research Article
doi.org/10.1002/batt.202500274

Chemistry
Europe
European Chemical
Societies Publishing

www.batteries-supercaps.org

Efficient Ion Diffusion and Stable Interphases for Designing Li$_2$S-Based Positive Electrodes of All-Solid-State Li/S Batteries

Yushi Fujita, Kota Motohashi, Atsushi Sakuda,* and Akitoshi Hayashi

All-solid-state lithium-ion batteries have promising applications due to their high energy density and safety. Lithium sulfide (Li$_2$S) is an attractive active material owing to its high theoretical capacity. The construction of composite positive electrodes has typically required electronic and lithium-ion conductive agents because of the insulating nature of Li$_2$S. Despite the existence of a multitude of electrode designs, the identification of a universally superior design remains elusive. This highlights the necessity for developing an evaluation method for Li$_2$S-based composite positive electrodes, aimed at deriving parameters that substantially influence electrode performance. Herein, guidelines are proposed for the development of Li$_2$S-based composite positive electrodes that can achieve a high charge–discharge capacity, rate performance, and cycling stability. Achieving higher performance necessitates both the diffusivity of lithium-ions during cycling and the interfacial stability with the sulfide solid electrolytes in the composite positive electrode. A systematic comparison of various combinations is conducted, and the results show that composite electrodes using Li$_2$S–LiI active material and Li$_3$PS$_4$–LiI sulfide solid electrolytes exhibit optimal performance. These findings provide a valuable foundation for the development of a novel Li$_2$S-based composite positive electrode with enhanced performance.

1. Introduction

All-solid-state batteries have promising applications because of their high energy density and safety. Lithium sulfide (Li$_2$S) is an attractive active material for positive electrodes.[1–5] The theoretical capacity of Li$_2$S is 1167 mAh g^{-1}, enabling the construction of batteries with a higher energy density than those of conventional oxide active materials. In addition, all-solid-state cells using Li$_2$S are first used in the charging process and it is not necessary to include Li sources in the negative electrode, which broadens the choice of materials for the negative electrode, such as carbon,[6] silicon,[7,8] and lithium anode-free systems.[9] However, Li$_2$S has low electronic and ionic conductivities.[10,11] To provide electronic and ionic conductions to Li$_2$S, conductive agents are typically mixed with Li$_2$S to form composite positive electrodes.[12,13] The redox reaction of Li$_2$S occurs at the three-phase interface among Li$_2$S, electronic, and ionic conductive agents. Increasing this three-phase interface enhances the charge–discharge capacity of Li$_2$S. In addition, Li$_2$S has a large energy barrier for activation,[14–16] and it is necessary to activate the redox reaction by constructing composites that can efficiently transport electrons and lithium-ions.[17,18]

Substantial research has been conducted over the past decade on Li$_2$S-based composite positive electrodes. Conductive carbons[19–22] and transition metal sulfides[23–32] have been predominantly utilized as the electron conduction pathway, and sulfide solid electrolytes (SE)[33–35] and lithium salts[36–39] have been utilized as ionic conduction pathways. In addition, the concept of bifunctional materials, comprising active materials and SEs, has gained considerable attention.[40–44] Nevertheless, in research on the development of such Li$_2$S-based composite positive electrodes, there is a clear need for the creation of electrodes that achieve even higher capacity, improved rate performance, and enhanced cycle life. Although a wide variety of electrode designs exist, it is currently unclear which electrode is ultimately superior because the experimental data providing the basis for the superiority are varied in each composite positive electrode. Therefore, it is necessary to establish an evaluation method for Li$_2$S-based composite positive electrodes and derive the parameters that have impacts on electrode performance, such as high capacity, high rate, and high cyclability.

Li$_2$S–LiI composite positive electrodes have been shown to be promising composites.[36,45–49] The all-solid-state cells with the composite electrodes exhibited a high charge–discharge capacity comparable to the theoretical capacity and an excellent rate and cycle performance of a 2C rate over 2000 cycles at 25 °C.[11] **Figure 1** shows an illustration of the all-solid-state cells using the Li$_2$S–LiI composite positive electrodes. The composite positive electrode consists of a nanocomposite and a sulfide SE. The nanocomposite is composed of Li$_2$S, LiI, and conductive carbon. The reason for the high performance of Li$_2$S–LiI composite positive electrodes has been investigated previously. First, LiI acts as a lithium-ion conductive pathway at the nanoscale and activated charge–discharge reactions.[50] This is an important factor in battery performance, and the lithium-ion diffusion changes

Y. Fujita, K. Motohashi, A. Sakuda, A. Hayashi
Department of Applied Chemistry
Graduate School of Engineering
Osaka Metropolitan University
1-1 Gakuen-cho, Naka-ku, Sakai, Osaka 599-8531, Japan
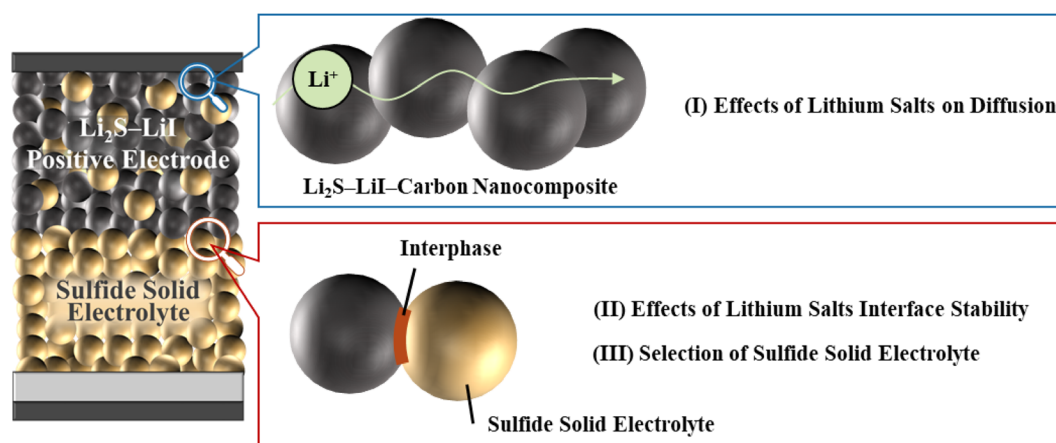*E-mail: saku@omu.ac.jp*

Figure 1. Schematic of all-solid-state cells using Li_2S-based composite positive electrodes and the study concept.

depending on the type of the added lithium salt (or a material that acts as a lithium-ion conductive pathway in the nanoscale).[39,51] Second, LiI is important to the stability of the interphase between the nanocomposite and sulfide SE. To overcome the activation barriers of Li_2S, and to obtain an even higher charge–discharge capacity, the all-solid-state cells using Li_2S-based composite positive electrodes have been tested beyond the electrochemically stable voltage range of sulfide SE.[17,52–54] The redox decomposition of sulfide SE significantly affects the cycle performance[17,52–54] and is a major issue. When LiI is included in the composite positive electrode, interphase layers are formed on the surface of the sulfide SEs, preventing excessive redox decomposition.[55] However, few studies have focused on the interface, and its formation is unclear in most cases. Moreover, the selection of the sulfide SEs would control the formation of the interphase.

In this study, a Li_2S-based composite positive electrode containing various lithium salts (denoted as LiX) is systematically compared, and a Li_2S-based positive electrode configuration is proposed to achieve a high capacity, rate performance, and cycle stability. The following three factors are particularly important for improving the performance of Li_2S-based composite positive electrodes: 1) the diffusion of lithium-ions in the nanocomposite of Li_2S–LiX and conductive carbons during cycling, 2) the interfacial stability between the nanocomposite and sulfide SE, and 3) the selection of the sulfide SE. Thus, diffusion coefficients are determined by electrochemical tests, the interface is observed by scanning electron microscopy (SEM) and energy-dispersive X-ray spectroscopy (EDS), and cell performances are compared for each type of sulfide SE.

2. Results and Discussion

2.1. Lithium-Ion Diffusion in Li_2S–LiX–Carbon Nanocomposite as an Active Material

Lithium salts are expected to act as a lithium-ion conductive pathway in the nanocomposite, assisting lithium-ion diffusion and redox kinetics of Li_2S. However, the relationship between the lithium salt used in the active materials and electrode performance is

not fully understood. At least among the lithium halides, all-solid-state cells with Li_2S-based composite positive electrodes exhibited different charge–discharge capacities depending on the lithium salt added.[11,56] Thus, the influence of the lithium salts on lithium-ion diffusion was first investigated. Previous studies have revealed the relationship between the oxidation tolerance of lithium salts and charge–discharge capacities, and lithium salts must have a higher oxidation tolerance than that of Li_2S to enhance battery performance.[39] Based on existing knowledge, lithium halides (LiF, LiCl, LiBr, and LiI) and lithium oxysalts (Li_2O, Li_3PO_4, Li_2SO_4, and Li_2SO_3) were selected as lithium salts in this study. The ionic conductivities of these lithium salts and Li_2S–LiX composites (Li_2S:LiX = 3:2 weight ratio) are summarized in **Table 1**.[39,51]

The ionic conductivity of LiX differed whereas those of Li_2S–LiX composites ranged from $\approx 10^{-7}$ to 10^{-6} S cm^{-1}. Therefore, the addition of lithium salts increased the ionic conductivity of Li_2S but the ionic conductivities of Li_2S–LiX composites were similar and not dependent on the selection of lithium salts. In addition, the battery performance at the start of the initial charge (e.g., within 100 mAh g^{-1} per Li_2S weight) is expected to be similar for all cells with Li_2S–LiX composites. Figure S1, Supporting Information, shows the X-ray diffraction (XRD) patterns of the Li_2S–LiX composites. The prepared samples were composite or

Table 1. Summary of the ionic conductivity of Li_2S, LiX, and Li_2S–LiX composites (Li_2S:LiX = 3:2 weight ratio).

LiX	Ionic conductivity at 25 °C/S cm^{-1}	Li_2S–LiX	Ionic conductivity at 25 °C/S cm^{-1}
Li_2S	$8.3 \times 10^{-9[11]}$		
LiF	Too low	Li_2S–LiF	8.1×10^{-8}
LiCl	$9.7 \times 10^{-8[39]}$	Li_2S–LiCl	$2.1 \times 10^{-6[11]}$
LiBr	$2.2 \times 10^{-7[39]}$	Li_2S–LiBr	$3.2 \times 10^{-6[11]}$
LiI	$3.2 \times 10^{-6[39]}$	Li_2S–LiI	$2.2 \times 10^{-6[11]}$
Li_2O	$1.3 \times 10^{-9[84]}$	Li_2S–Li_2O	1.9×10^{-6}
Li_3PO_4	Too low	Li_2S–Li_3PO_4	9.4×10^{-7}
Li_2SO_4	$4.8 \times 10^{-9[39]}$	Li_2S–Li_2SO_4	$2.0 \times 10^{-6[51]}$
Li_2SO_3	Too low	Li_2S–Li_2SO_3	$1.5 \times 10^{-7[51]}$

Batteries & Supercaps

Research Article
doi.org/10.1002/batt.202500274

Chemistry Europe
European Chemical
Societies Publishing

solid solutions.[11,39] Although some composites remain unreacted lithium salts, it is considered to have almost no adverse effect on the battery performance.

To investigate the lithium-ion diffusion during cycling, a galvanostatic intermittent titration technique (GITT) was performed. Typically, the composite positive electrode contains sulfide SEs to ensure ionic conduction at tens to hundreds of μm. However, the sulfide SEs can also react at the interface of conductive carbon and behave as active materials.[57–59] This causes lithium-ion diffusion by the redox reaction of Li_2S–LiX composites to overlap with that of sulfide SEs. Thus, the nanocomposite without sulfide SEs of Li_2S–LiX composites and vapor-grown carbon fiber (VGCF), which are electronic conductive agents, were directly used as a positive electrode layer to avoid the overlap. Charge–discharge tests using this type of composite electrode have been previously reported, demonstrating high capacity by adjusting charge–discharge conditions.[50] In addition, this composite can be evaluated as a planar electrode by applying the diffusion equation as follows[60–64]

$$D = \frac{4}{\pi t}\left(\frac{n_m V_m}{S}\right)^2\left(\frac{\Delta E_s}{\Delta E_t}\right)^2 \tag{1}$$

Here, D is the diffusion coefficient, t is the galvanostatic time (600 s), n_m is the molar concentration of Li in Li_2S, V_m is the molar volume of Li_2S–LiX–VGCF, S is the contact area between the composite positive electrode and the separator (0.785 cm^2), ΔE_s is the voltage difference between the open circuit voltages (OCVs) after the current and previous rests, and ΔE_t is the voltage difference

before and after performing GITT. **Figure 2**a,b shows the GITT curves, and Figure 2c,d plots the diffusion coefficients of the cells using Li_2S–VGCF and Li_2S–LiI–VGCF. The results of the cells using the other lithium salts are shown in Figure S2 and S3, Supporting Information. The cell with Li_2S–LiX–VGCF exhibited a higher capacity and lower overpotential than that with Li_2S–VGCF. This confirms that lithium salts act as ionic conductors and enhance the redox reaction of Li_2S. Interestingly, the changes in the diffusion coefficients during charging were similar for each lithium salt within the obtained capacity, suggesting that the diffusion coefficients reflect the diffusion by the redox reaction of Li_2S. To the best of our knowledge, this is the first time that diffusion coefficients originating from Li_2S have been observed. The charge–discharge mechanism of only Li_2S–LiI has already been elucidated by electrochemical measurements and structural analysis,[50] and it is expected that all cells in this study have similar charge–discharge mechanisms. The diffusion coefficients during discharging increased by adding lithium salts and similar profiles were observed for each lithium salt. The diffusion coefficient increased significantly at the end of the discharge process, in the region of the depth of discharge where Li_2S is formed.[50] This suggests that lithium-ion diffusion in Li_2S is faster than that in oxidative products, such as lithium polysulfides. Therefore, to achieve a high charge capacity, a lithium-ion conductive pathway in the nanoscale is essential to ensure ionic conduction of the oxidation products of Li_2S during cycling, rather than increasing the ionic conductivity of the positive electrode in advance before cycling.
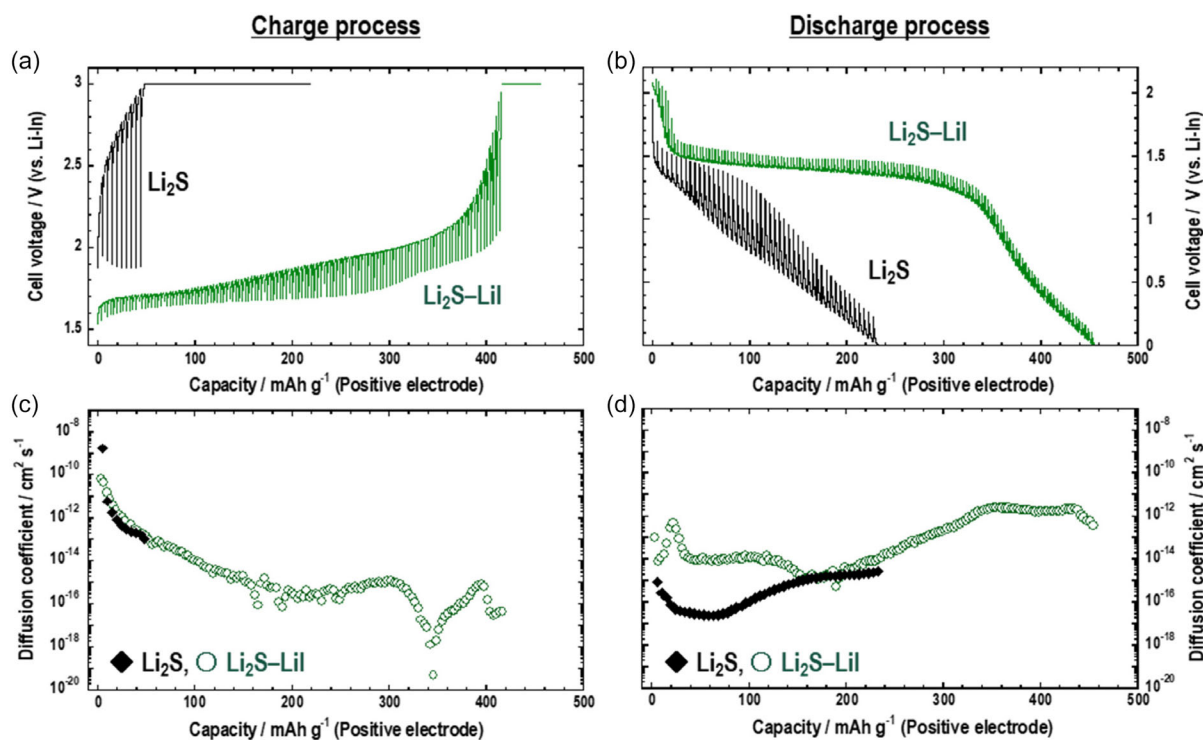

Figure 2. a,b) GITT plots and c,d) diffusion coefficients of all-solid-state cells (Li–In/Li_3PS_4/Li_2S–VGCF, and Li_2S–LiI–VGCF). The measurements were conducted at a C/30 rate (≈0.13 mA cm^{-2}) at 60 °C. GITT was performed for 10 min followed by a rest for 60 min. The weight of the positive electrode was ≈5 mg, corresponding to ≈3.2 mg cm^{-2} of Li_2S.

Batteries & Supercaps

Research Article
doi.org/10.1002/batt.202500274

Chemistry
Europe
European Chemical
Societies Publishing

Lithium-ion diffusion after charging can be also compared using the Warburg impedance obtained from electrochemical impedance spectroscopy (EIS). Warburg coefficients are calculated as follows.[50,65,66]

$$Z = A_w \omega^{-\frac{1}{2}}(1 - j) \quad (2)$$

Here, Z is an impedance obtained by EIS and A_w is the Warburg coefficient. Z is proportional to $\omega^{-\frac{1}{2}}$, and the slope of $Z/\omega^{-\frac{1}{2}}$ is the Warburg coefficient.[50,65,66] The Warburg coefficient is inverse to the diffusion coefficient,[65] suggesting the smaller the Warburg coefficient, the larger the diffusion coefficient. **Figure 3** shows a Nyquist plot of the all-solid-state cells with Li$_2$S–VGCF, Li$_2$S–LiBr–VGCF, and Li$_2$S–LiI–VGCF after charging. Figure S4 and S5, Supporting Information, show Nyquist plots of the all-solid-state cells with Li$_2$S–VGCF and all Li$_2$S–LiX–VGCF after charging, respectively, and the relationship between the square root of the reciprocal of the angular frequency and impedance of actual components at the frequency range of 0.1 to 0.01 Hz. **Table 2** lists the calculated Warburg coefficients. In the low-frequency range which indicates lithium-ion diffusion,[50,65,67] the Nyquist plots of the all-solid-state cell with Li$_2$S–LiI–VGCF exhibited a shorter tail than that of Li$_2$S–VGCF. The Warburg coefficient of Li$_2$S–LiI–VGCF was smaller than that of Li$_2$S–VGCF, indicating that lithium-ion diffusion of Li$_2$S–LiI–VGCF is faster than that of Li$_2$S–VGCF after charging. In addition, it is notable that the Warburg coefficients of Li$_2$S–Li$_2$SO$_4$–VGCF and Li$_2$S–Li$_2$SO$_3$–VGCF were smaller than that of Li$_2$S–LiI–VGCF. In a previous study, all-solid-state cells using Li$_2$S–Li$_2$SO$_4$–VGCF–SE and Li$_2$S–Li$_2$SO$_3$–VGCF–SE as a positive electrode exhibited high rate performance,[51] and the small Warburg coefficient of Li$_2$S–Li$_2$SO$_4$–VGCF and Li$_2$S–Li$_2$SO$_3$–VGCF in this study is consistent with the high rate performance. Thus, Li$_2$SO$_4$ and the related materials are promising for the development of high-performance Li$_2$S-based positive electrodes, and further material exploration is expected. However, the Warburg coefficient of Li$_2$S–LiBr–VGCF was larger than that of Li$_2$S–VGCF despite the all-solid-state cell with Li$_2$S–LiBr–VGCF exhibiting a higher capacity, smaller

Table 2. Warburg coefficients of all-solid-state cells using Li$_2$S–VGCF and Li$_2$S–LiX–VGCF.

Li$_2$S–LiX	$A_w/\Omega\ s^{1/2}$
Li$_2$S	1049
Li$_2$S–LiF	1017
Li$_2$S–LiCl	693
Li$_2$S–LiBr	1206
Li$_2$S–LiI	460
Li$_2$S–Li$_2$O	739
Li$_2$S–Li$_3$PO$_4$	903
Li$_2$S–Li$_2$SO$_4$	377
Li$_2$S–Li$_2$SO$_3$	408

overvoltage, and larger diffusion coefficients. Nyquist plots of the all-solid-state cells with Li$_2$S–LiBr–VGCF exhibited resistance components at a frequency range of $\approx$10 to 0.1 Hz, which originates from the interface resistance between active materials and SEs,[68,69] that is mainly the decomposition of LiBr. This profile has also been observed in the cell using Li$_2$S–LiBH$_4$–VGCF, where LiBH$_4$ is oxidatively decomposed.[39] After LiBr was decomposed at the ends of the charge process, the oxidative products of LiBr were no longer a lithium-ion conductive pathway in the nanocomposite and prevented from lithium-ion diffusion. In the subsequent discharge process, the oxidative products would be reduced to LiBr, which acts as an ionic conductor, leading to a high discharge capacity. However, the oxidation potential of LiI was also reached whereas A_w of the all-solid-state cells with Li$_2$S–LiI–VGCF was significantly smaller. A reason for this is that LiI acts as a redox mediator,[31,54,70] but LiBr does not. The electronic state of LiI in Li$_2$S–LiI–VGCF after charging was similar to that of the starting materials of LiI.[50] In summary, lithium salts act as ionic conductors to enhance the performance of Li$_2$S-based electrodes. In addition, it is important to ensure the ionic conductivity during the charge–discharge process, not only the initial ionic conductivity. LiI, Li$_2$SO$_4$, and Li$_2$SO$_3$ were found to be promising for lithium-ion diffusion.

2.2. Interphase between Li$_2$S–LiX–Carbon Nanocomposite and Sulfide Solid Electrolyte

Most all-solid-state cells with Li$_2$S-based composite positive electrodes have been cycled beyond the voltage at which sulfide SEs are electrochemically stable to overcome the large overpotential that occurs in the solid-state redox reaction of Li$_2$S[14–16] and achieve maximum charge–discharge capacity. This causes the decomposition of sulfide SEs and leads to cycle degradation. Therefore, the formation of a stable interphase between active materials and sulfide SEs is important to achieve stable cycling. It has been demonstrated that an amorphous interphase was formed during the initial charging between Li$_2$S–LiI–VGCF and Li$_3$PS$_4$ and the interphase protects sulfide SEs from excessive decomposition, leading to a long cycle life.[55] However, it has not been systematically investigated whether the interphase is formed for each lithium salt. Thus, in this section, SEM observations
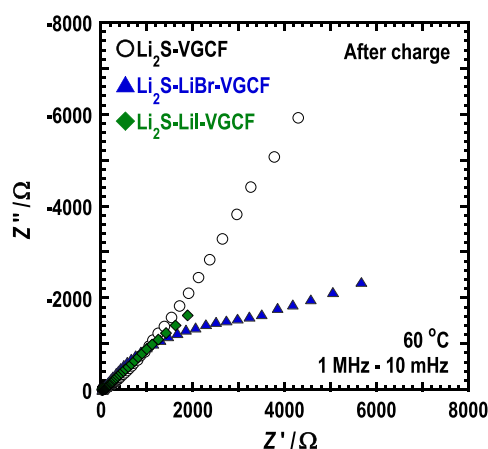

Figure 3. Nyquist plot of all-solid-state cells (Li–In/Li$_3$PS$_4$/Li$_2$S–VGCF, Li$_2$S–LiBr–VGCF, and Li$_2$S–LiI–VGCF) after charging. AC impedance measurements were conducted from 1 MHz to 10 mHz at 60 °C.

Batteries & Supercaps

Research Article
doi.org/10.1002/batt.202500274

Chemistry Europe
European Chemical
Societies Publishing

were conducted on the all-ssolid-state cell using Li₂S–LiX–VGCF as a positive electrode and Li₃PS₄ as a separator layer to determine whether the interphase was formed. Before interphase formation was determined, the oxidation voltage of lithium salts was investigated by linear sweep voltammetry (LSV), and cyclic voltammetry (CV) was measured for the all-solid-state cells using LiX–VGCF–Li₃PS₄ as a working electrode to investigate reversibility. In addition, the cycle performance was compared among the all-solid-state cells using Li₂S–VGCF–Li₃PS₄ and Li₂S–LiX–VGCF–Li₃PS₄ (LiX = LiF, LiCl, LiBr, LiI, Li₂O, Li₃PO₄, Li₂SO₄, and Li₂SO₃).

The oxidation voltage was examined for LiCl, LiBr, and LiI as representatives by LSV. Electrochemical characterizations such as LSV and CV have been used to investigate the electrochemical windows of SEs. The target SEs were mixed with conductive carbon, and the composite was used as a working electrode to obtain a large reaction current.[71] However, when the same cell configurations were applied (e.g., Li–In/LiCl/LiCl–VGCF) and the cells were assembled by pressing powders, the cell did not function because lithium salts have a low ionic conductivity (Table 1). A novel cell configuration for LSV tests has been reported and the redox potential of Li₂SO₄ has been successfully observed.[72] Thus, the same cell configuration was applied and the oxidation voltages of LiCl, LiBr, and LiI were investigated. **Figure 4**a–c shows

the LSV curves. The oxidation onset voltages (OOVs) of LiCl, LiBr, and LiI were 3.26, 2.75, and 2.18 V versus Li–In, respectively, which were similar to the calculated oxidation voltages.[52,53] In addition, the oxidation voltage of LiBr was also consistent with the plateau of the all-solid-state cells using Li₂S–LiBr–VGCF, as shown in Figure S2, Supporting Information.

CV was tested for the all-solid-state cells using LiX–VGCF–Li₃PS₄ as the working electrode. This cell configuration reflects the redox of both LiX and Li₃PS₄.[72] Figure 4d–f shows the CV curves of the all-solid-state cells using LiX–VGCF–Li₃PS₄ (LiX = LiCl, LiBr, and LiI) for three cycles, and Figure S6, Supporting Information, shows those using the other lithium salts. The CV curves of the all-solid-state cells using LiCl–VGCF–Li₃PS₄ (Figure 4d) and LiBr–VGCF–Li₃PS₄ (Figure 4e) showed reduction peaks mainly only in the first cycles. In contrast, those cells with LiI (Figure 4f) and Li₃PS₄–VGCF (Figure S6, Supporting Information) as the working electrodes exhibited hysteresis by both oxidation and reduction current peaks for three cycles, suggesting reversibility. This indicates that LiCl prevents reversible redox of Li₃PS₄ and forms a passivation layer on the surface of Li₃PS₄ because of the incompatibility of sulfides and chlorides,[73–77] although LiCl did not redox in the measured voltage range. LiBr is considered to behave as LiCl rather than LiI. In addition, in Figure S6, Supporting Information, the CV curves of
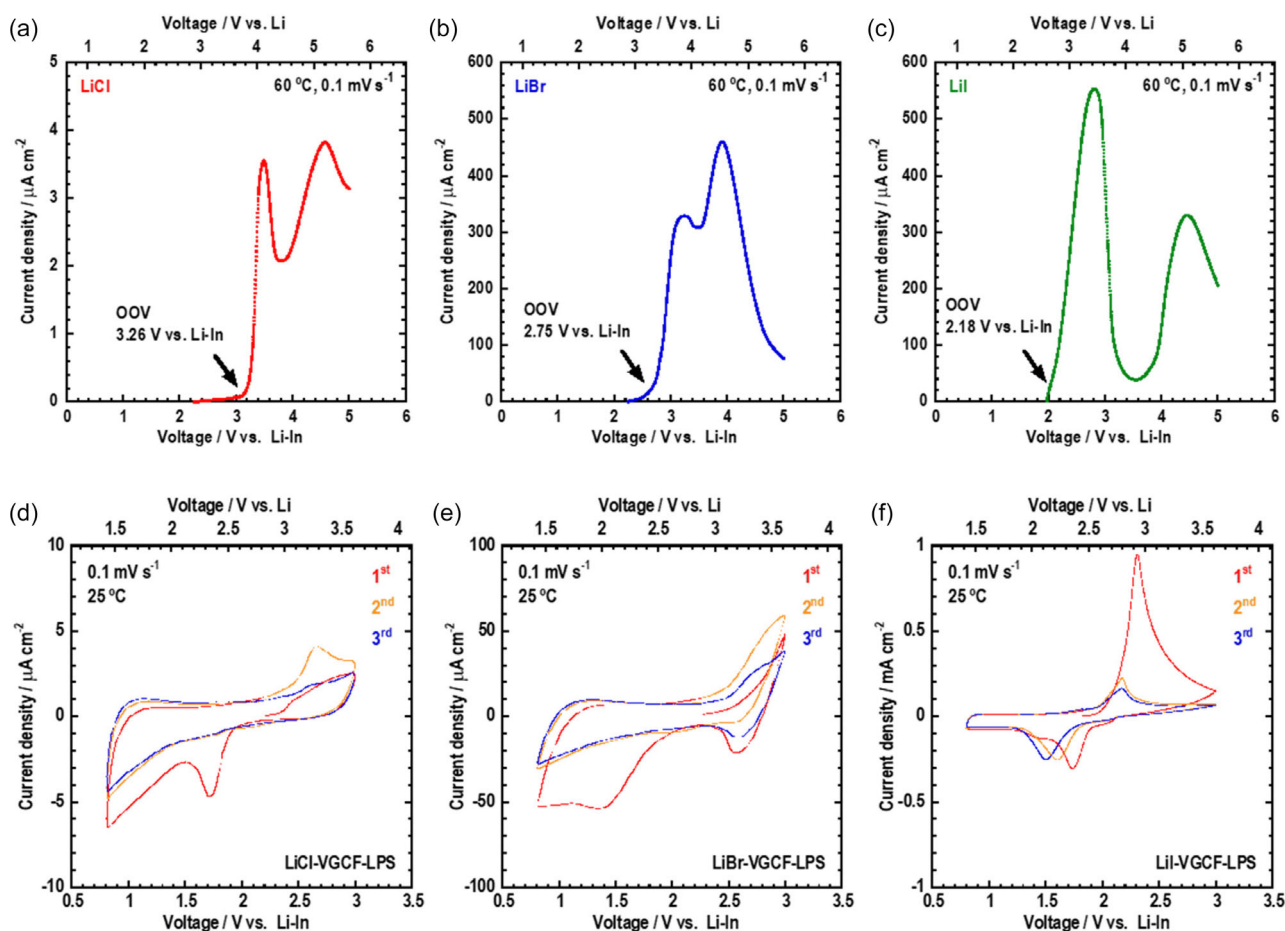

Figure 4. a–c) LSV curves of all-solid-state cells (Li–In/Li₃PS₄/90Li₃BO₃·10Li₂SO₄/Li₂X–VGCF–90Li₃BO₃·10Li₂SO₄ (LiX = LiCl, LiBr, and LiI)). The LSV measurements were conducted using an OCV to 5 V versus Li–In at 60 °C and 0.1 mV s⁻¹. d–f) CV curves of all-solid-state cells (Li–In/Li₃PS₄/LiX–VGCF–Li₃PS₄ (LiX = LiCl, LiBr, LiI)). The CV measurements were conducted from 0.8 to 3 V versus Li–In at 25 °C and 1 mV s⁻¹.

all-solid-state cells with Li_3PO_4 and Li_2SO_4 exhibited a similar profile to that observed for LiCl and unlike that observed for Li_2SO_3, which is relatively reversible, indicating the formation of passivation layers.

The interphase formation between the Li_2S–LiX–VGCF and sulfide SEs was investigated by SEM observations. Li_3PS_4 was selected at first due to its high ductility and simple composition.[78] All-solid-state cells (Li–In/Li_3PS_4/Li_2S–LiX–VGCF) were assembled and cross-sectional SEM observations were conducted on the pellet after charging. **Figure 5** shows the cross-sectional SEM-EDS images of the cells using Li_2S–VGCF and Li_2S–LiI–VGCF, and Figure S7 and S8, Supporting Information, show those of the other cells. The interphase layer was formed between the Li_2S–LiI–VGCF and Li_3PS_4 layers, as previously reported.[55] However, the clear interphase in μm width was not observed in the cell using the other lithium salts and without lithium salts. In addition, detailed SEM observations at nanoscale magnification revealed a characteristic region, presumed to be the interphase layer, only in the cells using Li_2SO_3. Figure S9, Supporting Information, shows the SEM-EDS images of Li_3PS_4/Li_2S–Li_2SO_3–VGCF. The interphase was observed to be several hundred nm in length on the Li_3PS_4 layer near the interface. All-solid-state cells using Li_2S–Li_2SO_3 exhibited excellent cycling performance over 1000 cycles,[51] and the observed interphase may act as a protective layer and lead to stable cycling. LiI and Li_2SO_3 appeared to have good compatibility with sulfide SEs, whereas other lithium halides and lithium oxysalts did not.

Figure 6 shows the cycle performance of the all-solid-state cells with Li_2S–LiX–VGCF–Li_3PS_4 composite positive electrodes, and Figure S10, S11, and S12, Supporting Information, show the charge–discharge curves and the Coulombic efficiencies. The all-solid-state cell using Li_2S–LiI–VGCF–Li_3PS_4 exhibited the highest charge–discharge capacity and stable cycling for 100 cycles. The cell with Li_2SO_3 also showed a high capacity and stable cycling. However, the cells with the other lithium salts showed either a low charge–discharge capacity or capacity degradation. LiI and
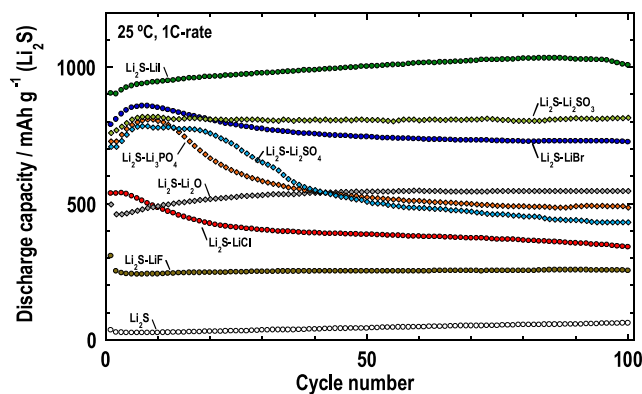
Figure 6. Cycle performance of all-solid-state cells (Li–In/Li_3PS_4/Li_2S–LiX–VGCF–Li_3PS_4 (LiX = LiF, LiCl, LiBr, LiI, Li_2O, Li_3PO_4, Li_2SO_4,[51] and Li_2SO_3[51])). The measurements were conducted at a 1C rate ($\approx$1.3 mA cm^{-2}) at 25 °C. The weight of the positive electrode was $\approx$3 mg, corresponding to $\approx$1 mg cm^{-2} of Li_2S.
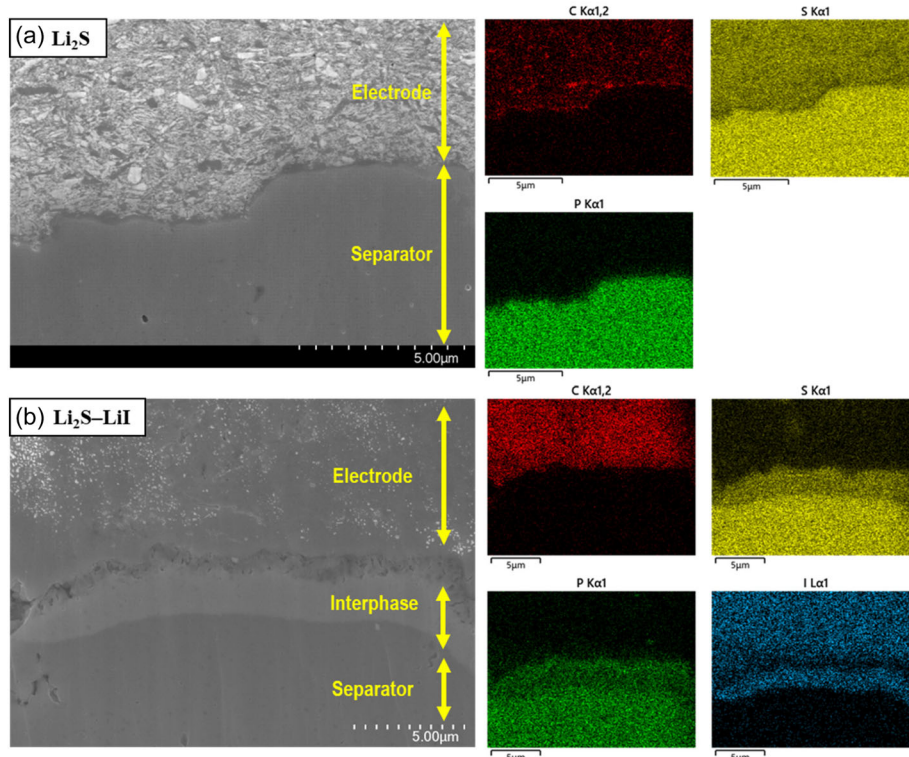
Figure 5. Cross-sectional SEM-EDS mappings of all-solid-state cells (Li–In/Li_3PS_4/ a) Li_2S–VGCF and b) Li_2S–LiI–VGCF) after charging. The measurements were conducted at a C/30 rate ($\approx$0.13 mA cm^{-2}) at 60 °C. GITT was performed for 10 min followed by a rest for 60 min.

Batteries & Supercaps

Research Article
doi.org/10.1002/batt.202500274

Chemistry Europe
European Chemical
Societies Publishing

Li_2SO_3 satisfy both relatively low Warburg coefficients, representing faster lithium-ion diffusion, and the formation of an interphase on the surface of sulfide SEs. Although the Li_2S–Li_2SO_4 composite exhibits the lowest Warburg coefficient, its electrochemical performance is inferior to that of Li_2S–LiI and Li_2S–Li_2SO_3 composites because Li_2S–Li_2SO_4 composites do not form the interphase with sulfide SEs. This indicates that the charge–discharge capacity, rate performance, and cyclability depend on lithium-ion diffusion during cycling and interphase formation with sulfide SEs. When comparing lithium salts that satisfy these two characteristics, higher ionic conductivity of lithium salts is advantageous in terms of improving performance. Furthermore, some cells increase capacity during the initial 10 cycles because of activation of active materials or Li_3PS_4. The degree of activation is considered to depend on the kinds of lithium salts and correlate with the results of the CV tests. Thus, to achieve even higher performance, it is important to design an excellent active material that has both the diffusivity of lithium ions during cycling and the interfacial stability with the sulfide SE.

2.3. Selection of Sulfide Solid Electrolyte

In the previous section, it was demonstrated that the stable interphase formation between active materials and sulfide SEs is important. The formation of the uniform interphase was achieved only by using LiI in this study. However, LiI must act as a lithium-ion

conductive pathway in the nanoscale in the Li_2S–LiI–VGCF nanocomposite. When large amounts of LiI were used by the formation of the interphase, ionic conduction pathways decreased in the active material, leading to poor lithium-ion diffusion. The interphase formation is controlled not only by active materials but also selection of sulfide SEs. In this study, sulfide SEs with halogen of argyrodite Li-P-S-Cl crystals (LPSC) and $2Li_3PS_4$·LiI glasses (LPSI) were compared because they have a high ionic conductivity of $>10^{-3}$ S cm^{-1}. To investigate the interphase formation between Li_2S–LiI–VGCF and LPSC or LPSI, the charge tests were performed using the cell (Li–In/SE/Li_2S–LiI–VGCF (SE = LPSC or LPSI)), and SEM observations were conducted as in the previous section. **Figure 7**a,b shows cross-sectional SEM images and EDS mappings of the cells after charging. In the cell using LPSC, an interphase of several micrometer thicknesses was formed several micrometers from the Li_2S–LiI–VGCF electrode (described as "I-rich phase" in Figure 7a). Interestingly, the interphase had iodide species but did not include chloride species. This indicates that iodine and chlorine have poor compatibility and that the interphase was forcibly formed in an area with a locally low chloride species content. As the LPSC layer is not completely covered by the interphase, the redox decomposition of LPSC will cause cycle degradation of the all-solid-state cell. In addition, large horizontal cracks were observed in the electrolyte layer, rather than between the electrode and the electrolyte layers. Furthermore, many voids were observed in the LPSC layers. This is because
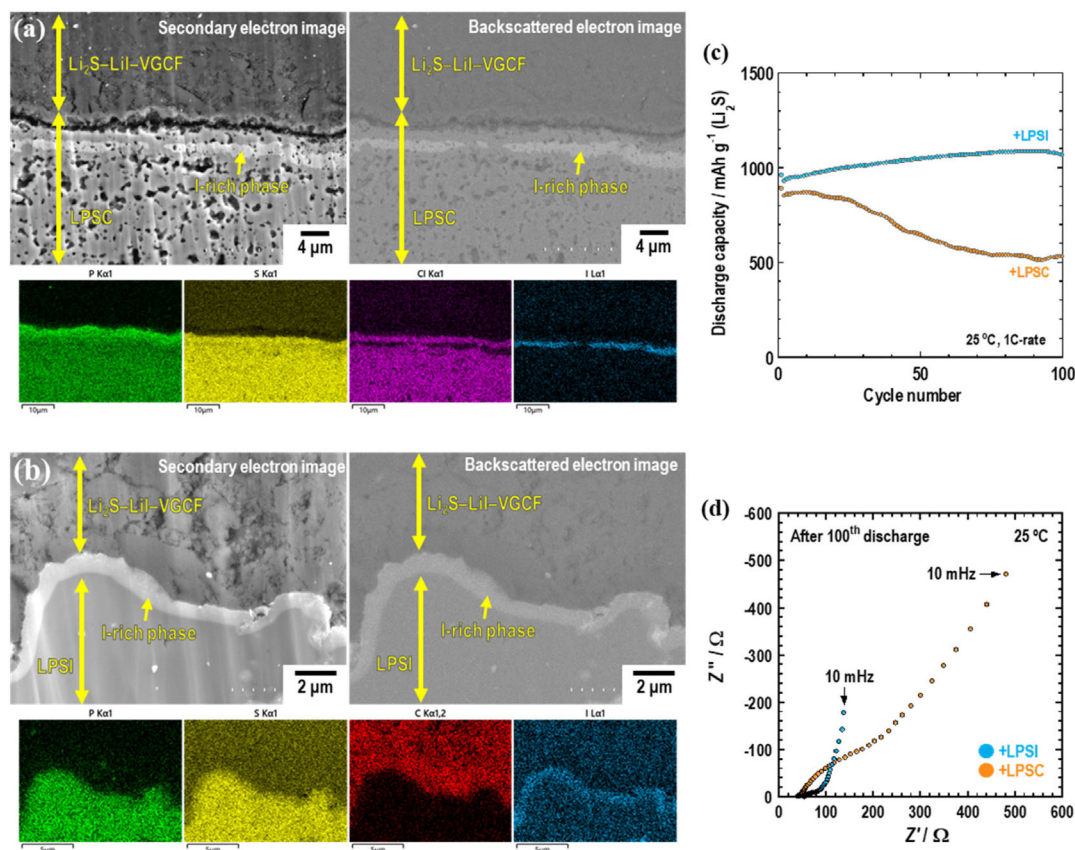

Figure 7. Cross-sectional SEM-EDS mappings of SE/Li_2S–LiI–VGCF interface (SE = a) Li-P-S-C crystals (LPSC) or b) $2Li_3PS_4$·LiI glass (LPSI)) after charging. c) Cycle performance of all-solid-state cells (Li–In/SE/Li_2S–LiI–VGCF–SE (SE = LPSC or LPSI). The measurements were conducted at a 1C rate ($\approx$1.3 mA cm^{-2}) at 25 °C. The weight of the positive electrode was $\approx$3 mg, corresponding to $\approx$1 mg cm^{-2} of Li_2S. d) Nyquist plot of the cells after the 100th discharging.

of the mechanical failure of LPSC.[79] These factors cause cycle degradation in all-solid-state cells and are discussed subsequently. In contrast, in the cell with LPSI as shown in Figure 7b, the interphase formed between the Li_2S–LiI–VGCF and LPSI layer without cracks. The EDS mappings in the interphase were brighter than those in the LPSI layer, suggesting that the interphase is more LiI-rich LPSI than the reported LPSI.[80–82] When 33 mol% of LiI was included in the SE layer, it was insufficient for the formation of the interphase, which means the iodide species were provided from the Li_2S–LiI–VGCF composite. In addition, the thickness of the formed interphase between the Li_2S–LiI–VGCF and LPSI is thinner than that of the Li_2S–LiI–VGCF and Li_3PS_4 (see Figure 5b). This suggests that the thickness of the interphase can be controlled by the amount of LiI added to LPSI. Furthermore, to avoid the provision of LiI from electrodes, LiI--coating on active materials or sulfide SEs would be effective.[83]

Figure 7c shows the cycle performance of the all-solid-state cells (Li–In/SE/Li_2S–LiI–VGCF–SE (SE = LPSC or LPSI). Figure S13, Supporting Information, shows charge–discharge curves and Coulombic efficiency. The cell with LPSI showed stable cycling whereas that with LPSC showed capacity degradation. Owing to the interphase formation and better mechanical properties of LPSI, the all-solid-state cell with LPSI showed a high battery performance but that with LPSC did not. Figure 7d shows the Nyquist plot of both cells after the 100th discharge. The cell with LPSI showed a shorter tale in the low-frequency range than that with LPSC, suggesting faster diffusion.[50,65,67] In addition, the cells with LPSC have resistance components at a frequency range of ≈ 10 to 0.1 Hz, which originate from interface resistance between active materials and SEs,[68,69] which is mainly the decomposition of LPSC. Redox decomposition of LPSC is a reason for capacity degradation. Therefore, at present, LPSI is the most suitable sulfide SE for the Li_2S-based composite positive electrode, following ionic conductivity, interphase formation, and mechanical properties.

3. Conclusion

The objective of this study was to establish guidelines for the development of a novel Li_2S-based composite positive electrode that would achieve a high charge–discharge capacity, rate performance, and cycling stability. Therefore, this study conducted a comparative analysis of lithium-ion diffusion during the cycling process, observed the interphase formation between active materials and sulfide SEs, and selected the sulfide SE necessary for achieving high performance in the Li_2S–LiX–VGCF–SE composite positive electrode. Lithium-ion diffusion during cycling was compared by GITT tests and EIS, showing that LiI, Li_2SO_4, and Li_2SO_3 exhibited superior lithium-ion diffusion. The thick interphase was formed in the cell using Li_2S–LiI–VGCF. The all-solid-state using the Li_2S–LiI–VGCF–Li_3PS_4 showed the highest charge–discharge capacity in those using the other lithium salts and exhibited stable cycling. This indicates that both fast lithium-ion diffusion during cycling and interphase formation are necessary to achieve a high charge–discharge capacity, rate performance, and cycling stability. As a sulfide SE, LPSC, and LPSI were compared, showing that LPSI is superior to LPSC because of ionic conductivity, interphase

formation, and mechanical properties. Thus, the Li_2S–LiI–VGCF–LPSI composite is the best of those investigated in this study. These results are helpful for the development of a novel Li_2S-based composite positive electrode with further high performance.

4. Experimental Section

Preparation of Solid Electrolytes

All procedures were conducted in a dry Ar atmosphere. Sulfide SEs and oxide SEs were used in this study. The sulfide SEs were Li_3PS_4 glass, argyrodite Li-P-S-Cl SEs (Mitsui Kinzoku), and $2Li_3PS_4 \cdot LiI$ glass. Two different sizes of Li_3PS_4 glass (5 and 20 μm) were prepared to use different sizes for composite positive electrode layers and separator, which are important for achieving high performance.[49] The Li_3PS_4 glass was prepared by a mechanochemical process and further wet milling of milled Li_3PS_4 glass with dehydrated heptane and dibutyl ether under the same milling conditions. The starting materials of Li_2S (99.9%, Mitsuwa Chemicals Co., Ltd.) and P_2S_5 (99%, Sigma–Aldrich) were weighted in the stoichiometric composition of 75:25 mol%. The weighted materials were placed into a ZrO_2 pot (250 mL) with ZrO_2 balls (450 mg, diameter = 4 mm). A large ball mill apparatus and ZrO_2 pots were used because Li_3PS_4 requires more sample material than the other materials. Mechanochemical milling was conducted using a ball mill apparatus (Fritsch, Pulverisette 5 classic line) at a rotation speed of 210 rpm of 70 h. The energy applied under the ball mill condition was comparable to that used for small-scale synthesis. The $2Li_3PS_4 \cdot LiI$ glass was prepared using the obtained Li_3PS_4 glass and LiI (99.999%, Sigma–Aldrich). The Li_3PS_4 glass and LiI were weighed in the stoichiometric composition of 2:1 (molar ratio) and mixed using an agate mortar and pestle. The mixed materials were placed into a ZrO_2 pot (45 mL) with ZrO_2 balls (90 mg, diameter = 4 mm). Mechanochemical milling was conducted using a planting ball mill apparatus (Fritsch, Pulverisette 7 classic line) at a rotation speed of 510 rpm of 20 h. $90Li_3BO_3 \cdot 10Li_2SO_4$ glass-ceramic was used in all-solid-state cells for LSV.[72] The starting materials of Li_2SO_4 were obtained by drying $Li_2SO_4 \cdot H_2O$ (99.0%, FUJIFILM Wako Chem. Co.) at 300 °C for 2 h in vacuum. Li_3BO_3 (99.9%, TOSHIMA Co., Ltd.) and Li_2SO_4 were mixed by an agate mortar and pestle and placed into a ZrO_2 pot (45 mL) with ZrO_2 balls (65 mg, diameter = 5 mm). Mechanochemical milling was conducted using a ball mill apparatus (Fritsch, Pulverisette 7 classic line) at a rotation speed of 370 rpm of 100 h. The milled samples were heat-treated at 270 °C for 2 h to form glass-ceramic. The ionic conductivity at 25 °C of each SE was approximately $\approx 10^{-4}$ S cm^{-1} (Li_3PS_4 glass), $\approx 10^{-3}$ S cm^{-1} (LPSC and LPSI), and $\approx 10^{-6}$ S cm^{-1} ($90Li_3BO_3 \cdot 10Li_2SO_4$ glass-ceramic), respectively.

Preparation of Composite Positive Electrodes

Three types of composite electrodes were fabricated in this study: 1) a nanocomposite composed of Li_2S, lithium salt, and VGCF (manufactured by Resonac HD) (Li_2S–LiX–VGCF); 2) positive electrodes further added to the above SE (Li_2S–LiX–VGCF–SE); and 3) a working electrode for LSV and CV with lithium salt, VGCF, and SE (described as LiX–VGCF–SE). VGCF was dried at 160 °C for 24 h in a vacuum before mixing with the other materials. The following lithium salts (LiX) were used: LiF (99.98%, Sigma–Aldrich), LiCl (99.98%, Sigma–Aldrich), LiBr (99.999%, Sigma–Aldrich), LiI (99.999%, Sigma–Aldrich), Li_2O (99.9%, Furuuchi Chem.), Li_3PO_4 (99%, Kojundo Chem.), Li_2SO_4, and Li_2SO_3. Li_2O was dried at 300 °C for 12 h in a vacuum before mixing with the other materials. Li_2SO_3 was obtained by drying $Li_2SO_3 \cdot nH_2O$ (Mitsuwa Chemicals Co., Ltd.) at 200 °C for 10 h in a vacuum.[51]

The Li_2S–LiX–VGCF nanocomposites were prepared using the following two steps. First, Li_2S (99.9%, Mitsuwa Chemicals Co., Ltd.) and LiX

were ball-milled with ZrO_2 balls (28.8 g, diameter = 4 mm) in a ZrO_2 pot (45 mL) using a ball mill apparatus (Fritsch, Pulverisette 7 classic line) at a rotation speed of 510 rpm of 10 h. Second, the obtained Li_2S–LiX composite and VGCF were mixed using an agate mortar and pestle and ball-milled under the same conditions. The weight ratio of Li_2S, LiX, and VGCF was 3:2:1. An Li_2S–VGCF nanocomposite was also prepared in the same procedure with a weight ratio of 3:1. The Li_2S–LiX–VGCF–SE composite positive electrodes were prepared by mixing the Li_2S–LiX–VGCF nanocomposites and sulfide SEs. A ball mill apparatus (Fritsch, Pulverisette 23) was used for mixing, which was moderately mixed and similar to using an agate mortar and pestle, and the conditions were 20 Hz for 30 min. Li_3PS_4 glass, LPSC crystal, and $2Li_3PS_4 \cdot LiI$ glass were used for the sulfide SE in the composite positive electrode. The weight ratio of Li_2S, LiX, VGCF, and sulfide SE was 3:2:1:4. An Li_2S–VGCF–SE composite was also prepared in the same procedure with a weight ratio of 3:1:6. The LiX–VGCF–SE composite was prepared in the same manner as the Li_2S–LiX–VGCF–SE composite. $90Li_3BO_3 \cdot 10Li_2SO_4$ glass-ceramic or Li_3PS_4 glass was used for the SE in the composite. The weight ratio of LiX, VGCF, and $90Li_3BO_3 \cdot 10Li_2SO_4$ glass-ceramic was 9:1:10, and the weight ratio of LiX, VGCF, and Li_3PS_4 glass was 9:1:5. An active material is Li_2S for charge–discharge tests and is lithium salts for CV and LSV tests.

Cell Assembly

All-solid-state cells were assembled for galvanostatic charge–discharge tests, LSV, and CV. For the charge–discharge tests, all-solid-state cells (Li–In/SE/Li_2S–LiX–VGCF or Li_2S–LiX–VGCF–SE) were assembled. Solid electrolytes (80 mg) were placed into a polycarbonate tube (diameter = 10 mm) and pressed moderately. The Li_2S–LiX–VGCF ($\approx$5 mg) or Li_2S–LiX–VGCF–SE (3 mg) were placed on the surface of the separator layer and pressed together at 360 MPa for 5 min. Li foil (diameter = 6 mm, thickness = 250 μm) and In foil (diameter = 8 mm, thickness = 300 μm) were placed on the other side of the surface of the separator layer and pressed together at 36 MPa for 2 min. Stainless steel rods were used as current correctors. The assembled all-solid-state cells were strained by homemade flames and the applied pressure was >50 MPa. The LSV cells (Li–In/Li_3PS_4 glass/$90Li_3BO_3 \cdot 10Li_2SO_4$ glass-ceramic/ LiX–VGCF–$90Li_3BO_3 \cdot 10Li_2SO_4$ glass-ceramic) were assembled using the same procedure as in a previous study.[72] In a separator layer, the Li_3PS_4 (50 mg) was placed on the counter electrode, and $90Li_3BO_3 \cdot 10Li_2SO_4$ glass-ceramic (20–30 mg) was placed on the working electrode side. The working electrode (LiX–VGCF–$90Li_3BO_3 \cdot 10Li_2SO_4$ glass-ceramic) was 10 mg. Li–In alloy was prepared by attaching a Li metal strip (3 mg) to the In foil (110 mg) to prevent potential changes caused by a large deviation in the Li–In composition during LSV measurements. The CV cells (Li–In/Li_3PS_4 glass/LiX–VGCF–Li_3PS_4 glass) were assembled using the same procedure as that for all-solid-state cells for the charge–discharge tests. The LiX–VGCF–Li_3PS_4 glass composite was 10 mg and the Li–In alloys were the same as those used for the LSV tests.

Electrochemical Tests

Galvanostatic cycling tests, GITT, EIS, LSV, and CV were performed. Galvanostatic cycling tests were performed using a charge–discharge device (BTS-2004, Nagano Co.) at 25 °C and a 1C rate ($\approx$1 mA cm^{-2}). GITT was performed using a potentiostat/galvanostat (Solartron CellTest 1470 E). GITT was performed for 10 min followed by a rest of 60 min at 60 °C and a C/30 rate ($\approx$0.1 mA cm^{-2}). EIS for all-solid-state cells was performed using an impedance analyzer (SI-1287 and 1255B, Solartron Analytical) at 10^6 to 0.01 Hz and 10 mV. EIS was performed to determine ionic conductivity using an impedance analyzer (SI-1260, Solartron Analytical) at 10^7 to 0.1 Hz and 10 mV. LSV and CV were performed using a potentiostat (VersaSTAT 3, AMETEK, Inc.). The condition of LSV was from an OCV to 5 V versus Li–In (5.62 V versus Li$^+$/Li) at a

scan rate of 0.1 mV s^{-1} at 60 °C. The condition of CV was from 0.8 to 3 V versus Li–In (1.42 to 3.62 V versus Li$^+$/Li) at a scan rate of 1 mV s^{-1} at 25 °C for three cycles.

Structural Characterization

XRD was conducted using an X-ray diffractometer (SmartLab, Rigaku) with Cu Kα radiation. Powder samples were sealed in an airtight container with a polymer film window. Diffraction data were collected in the 2θ range of 5–80° at a scan rate of 10° min^{-1} with a step size of 0.02°. SEM-EDS was conducted on the cross section of positive electrodes. Cross sections were prepared using an Ar$^+$ ion milling system (IM4000; Hitachi High-Technologies Corp.) before SEM-EDS observations using a field-emission SEM (FE-SEM, SU-8220; Hitachi High Technologies Corp.) and an EDS system (EMAXEvolution X-MAX, Horiba Ltd.).

Conflict of Interest

The authors declare no conflict of interest.

Author Contributions

Yushi Fujita: conceptualization (lead); formal analysis (lead); investigation (lead); writing—original draft (lead). **Kota Motohashi**: writing—review and editing (equal). **Atsushi Sakuda**: funding acquisition (equal); supervision (lead); writing—review and editing (lead). **Akitoshi Hayashi**: funding acquisition (equal); supervision (equal); writing—review and editing (equal).

Data Availability Statement

The data that support the findings of this study are available from the corresponding author upon reasonable request.

[1] T. Liu, R. Liu, C. Lu, W. Song, *Adv. Sustain. Syst.* **2024**, 2400555. https://doi.org/10.1002/adsu.202400555.

[2] J. Lee, C. Zhao, C. Wang, A. Chen, X. Sun, K. Amine, G.-L. Xu, *Chem. Soc. Rev.* **2024**, *53*, 5264.

[3] W. Qian, Y. Guo, W. Zuo, X. Wu, L. Zhang, *Mater. Chem. Front.* **2024**, *8*, 2556.

[4] D. S. Baji, S. Kannan, P. B. Madambikattil, A. Thirumurugan, M. K. Sharma, R. K. Pai, A. Ramadoss, S. Nair, D. Santhanagopalan, *J. Energy Storage* **2024**, *100*, 113412.

[5] F. Liang, S. Wang, Q. Liang, A. Zhong, C. Yang, J. Qian, H. Song, R. Chen, *Adv. Energy Mater.* **2024**, *14*, 2401959.

[6] J. C. Verduzco, B. Bettes, Q. Hu, E. E. Marinero, *Ionics* **2023**, *29*, 439.

[7] A. Franco Gonzalez, N.-H. Yang, R.-S. Liu, *J. Phys. Chem. C Nanomater. Interfaces* **2017**, *121*, 27775.

[8] H. Huo, J. Janek, *ACS Energy Lett.* **2022**, *7*, 4005.

[9] P. Zhao, J. Pan, D. Zhang, Y. Tang, Z. Tai, Y. Liu, H. Gao, F. Huang, *Batteries* **2023**, *9*, 381.

[10] K. Zhang, L. Wang, Z. Hu, F. Cheng, J. Chen, *Sci. Rep.* **2014**, *4*, 6467.

[11] T. Hakari, A. Hayashi, M. Tatsumisago, *Adv. Sustainable Syst.* **2017**, *1*, 1700017.

[12] M. Nagao, A. Hayashi, M. Tatsumisago, *J. Mater. Chem.* **2012**, *22*, 10015.

[13] M. Nagao, A. Hayashi, M. Tatsumisago, T. Ichinose, T. Ozaki, Y. Togawa, S. Mori, *J. Power Sources* **2015**, *274*, 471.

[14] Y. Yang, G. Zheng, S. Misra, J. Nelson, M. F. Toney, Y. Cui, *J. Am. Chem. Soc.* **2012**, *134*, 15387.

[15] H. Ye, M. Li, T. Liu, Y. Li, J. Lu, *ACS Energy Lett.* **2020**, *5*, 2234.

[16] J. T. Kim, H. Su, Y. Zhong, C. Wang, H. Wu, D. Zhao, C. Wang, X. Sun, Y. Li, *Nat Chem. Eng.* **2024**, *1*, 400.

[17] S. Ohno, W. G. Zeier, *Acc. Mater. Res.* **2021**, *2*, 869.

[18] J. Gao, Y. Gao, J. Hao, X. Sun, F. Zhao, Y. Zhang, W. Si, J. Wu, *Small* **2024**, *20*, e2404171.

[19] F. Han, J. Yue, X. Fan, T. Gao, C. Luo, Z. Ma, L. Suo, C. Wang, *Nano Lett.* **2016**, *16*, 4521.

[20] H. Yan, H. Wang, D. Wang, X. Li, Z. Gong, Y. Yang, *Nano Lett.* **2019**, *19*, 3280.

[21] M. Jiang, G. Liu, Q. Zhang, D. Zhou, X. Yao, *ACS Appl. Mater. Interfaces* **2021**, *13*, 18666.

[22] Y. Yu, B. Singh, Z. Yu, C. Y. Kwok, I. Kochetkov, L. F. Nazar, *Adv. Energy Mater.* **2024**, *14*, 2400845.

[23] J. Balach, J. Linnemann, T. Jaumann, L. Giebeler, *J. Mater. Chem. A Mater. Energy Sustain.* **2018**, *6*, 23127.

[24] R. Brec, A. Dugast, A. Le Mehauté, *Mater. Res. Bull.* **1980**, *15*, 619.

[25] K. Takada, Y. Kitami, T. Inada, A. Kajiyama, M. Kouguchi, S. Kondo, M. Watanabe, M. Tabuchi, *J. Electrochem. Soc.* **2001**, *148*, A1085.

[26] A. Sakuda, T. Takeuchi, K. Okamura, H. Kobayashi, H. Sakaebe, K. Tatsumi, Z. Ogumi, *Sci. Rep.* **2014**, *4*, 4883.

[27] A. Sakuda, T. Takeuchi, M. Shikano, H. Sakaebe, H. Kobayashi, *Front. Energy Res.* **2016**, *4*, 19.

[28] Y. Kawasaki, H. Tsukasaki, T. Ayama, S. Mori, M. Deguchi, M. Tatsumisago, A. Sakuda, A. Hayashi, *ACS Appl. Energy Mater.* **2021**, *4*, 20.

[29] K. Takada, T. Inada, A. Kajiyama, M. Kouguchi, S. Kondo, M. Watanabe, *J. Power Sources* **2001**, *97–98*, 762.

[30] H. Gamo, K. Hikima, A. Matsuda, *ACS Omega* **2023**, *8*, 45557.

[31] P. Yu, S. Sun, C. Sun, C. Zeng, Z. Hua, N. Ahmad, R. Shao, W. Yang, *Adv. Funct. Mater.* **2024**, *34*, 2306939.

[32] K. Hikima, F. Fujii, H. Gamo, H. Tsukasaki, S. Mori, T. Watanabe, K. Yamamoto, Y. Uchimoto, H. Muto, A. Matsuda, *J. Phys. Chem. C* **2023**, *127*, 13511.

[33] A. Hayashi, S. Hama, T. Minami, M. Tatsumisago, *Electrochem. commun.* **2003**, *5*, 111.

[34] R. Mercier, J.-P. Malugani, B. Fahys, G. Robert, *Solid State Ionics* **1981**, *5*, 663.

[35] H.-J. Deiseroth, S.-T. Kong, H. Eckert, J. Vannahme, C. Reiner, T. Zaiss, M. Schlosser, *Angew. Chem. Int. Ed Engl.* **2008**, *47*, 755.

[36] H. Wan, B. Zhang, S. Liu, J. Zhang, X. Yao, C. Wang, *Nano Lett.* **2021**, *21*, 8488.

[37] J. Ding, Y. Fujita, H. Tsukasaki, H. Nakajima, A. Sakuda, A. Hayashi, S. Mori, *ACS Appl. Energy Mater.* **2023**, *6*, 9737.

[38] Y. Fujita, A. Sakuda, Y. Hasegawa, M. Deguchi, K. Motohashi, D. Jiong, H. Tsukasaki, S. Mori, M. Tatsumisago, A. Hayashi, *Small* **2023**, *19*, 2302179.

[39] T. Hakari, Y. Fujita, M. Deguchi, Y. Kawasaki, M. Otoyama, Y. Yoneda, A. Sakuda, M. Tatsumisago, A. Hayashi, *Adv. Funct. Mater.* **2021**, *32*, 2106174.

[40] T. Shigedomi, Y. Fujita, T. Kishi, K. Motohashi, H. Tsukasaki, H. Nakajima, S. Mori, M. Tatsumisago, A. Sakuda, A. Hayashi, *Chem. Mater.* **2022**, *34*, 9745.

[41] W. Pan, K. Yamamoto, T. Matsunaga, T. Watanabe, M. Kumar, N. Thakur, T. Uchiyama, M. Uesugi, A. Takeuchi, A. Sakuda, A. Hayashi, M. Tatsumisago, Y. Uchimoto, *Batter. Supercaps* **2024**, *7*, e202300427.

[42] M. Li, T. Liu, Z. Shi, W. Xue, Y.-S. Hu, H. Li, X. Huang, J. Li, L. Suo, L. Chen, *Adv. Mater.* **2021**, *33*, e2008723.

[43] L. Cui, S. Zhang, J. Ju, T. Liu, Y. Zheng, J. Xu, Y. Wang, J. Li, J. Zhao, J. Ma, J. Wang, G. Xu, T.-S. Chan, Y.-C. Huang, S.-C. Haw, J.-M. Chen, Z. Hu, G. Cui, *Nat. Energy* **2024**, *9*, 1084.

[44] E. McCalla, *Nat. Energy* **2024**, *9*, 1056.

[45] A. Jodlbauer, K. Hogrefe, B. Gadermaier, H. M. R. Wilkening, *Small Sci.* **2024**, *4*, 2400199.

[46] R. Xu, J. Yue, S. Liu, J. Tu, F. Han, P. Liu, C. Wang, *ACS Energy Lett.* **2019**, *4*, 1073.

[47] M. Liu, C. Wang, C. Zhao, E. van der Maas, K. Lin, V. A. Arszelewska, B. Li, S. Ganapathy, M. Wagemaker, *Nat. Commun.* **2021**, *12*, 5943.

[48] J. T. Kim, A. Rao, H.-Y. Nie, Y. Hu, W. Li, F. Zhao, S. Deng, X. Hao, J. Fu, J. Luo, H. Duan, C. Wang, C. V. Singh, X. Sun, *Nat. Commun.* **2023**, *14*, 6404.

[49] Y. Fujita, K. Münch, T. Asakura, K. Motohashi, A. Sakuda, J. Janek, A. Hayashi, *Chem. Mater.* **2024**, *36*, 7533.

[50] Y. Fujita, T. Hakari, A. Sakuda, M. Deguchi, Y. Kawasaki, H. Tsukasaki, S. Mori, M. Tatsumisago, A. Hayashi, *ACS Appl. Energy Mater.* **2022**, *5*, 9429.

[51] Y. Fujita, K. Motohashi, J. Ding, H. Tsukasaki, S. Mori, A. Sakuda, A. Hayashi, *ACS Appl. Energy Mater.* **2024**, *7*, 5447.

[52] Y. Zhu, X. He, Y. Mo, *ACS Appl. Mater. Interfaces* **2015**, *7*, 23685.

[53] W. D. Richards, L. J. Miara, Y. Wang, J. C. Kim, G. Ceder, *Chem. Mater.* **2016**, *28*, 266.

[54] H. Gamo, K. Hikima, A. Matsuda, *Chem. Mater.* **2022**, *34*, 10952.

[55] Y. Fujita, J. Ding, H. Kowada, S. Mori, K. Motohashi, A. Sakuda, A. Hayashi, *ACS Appl. Energy Mater.* **2025**, *8*, 2192.

[56] T. Shigedomi, Y. Fujita, K. Motohashi, M. Tatsumisago, A. Sakuda, A. Hayashi, *ACS Appl. Mater. Interfaces* **2024**, *16*, 20542.

[57] T. Hakari, M. Deguchi, K. Mitsuhara, T. Ohta, K. Saito, Y. Orikasa, Y. Uchimoto, Y. Kowada, A. Hayashi, M. Tatsumisago, *Chem. Mater.* **2017**, *29*, 4768.

[58] C. Yu, S. Ganapathy, N. J. J. de Klerk, I. Roslon, E. R. H. van Eck, A. P. M. Kentgens, M. Wagemaker, *J. Am. Chem. Soc.* **2016**, *138*, 11192.

[59] D. H. S. Tan, E. A. Wu, H. Nguyen, Z. Chen, M. A. T. Marple, J.-M. Doux, X. Wang, H. Yang, A. Banerjee, Y. S. Meng, *ACS Energy Lett.* **2019**, *4*, 2418.

[60] W. Weppner, R. A. Huggins, *J. Electrochem. Soc.* **1977**, *124*, 1569.

[61] K. Mizushima, P. C. Jones, P. J. Wiseman, J. B. Goodenough, *Mater. Res. Bull.* **1980**, *15*, 783.

[62] P. Prosini, *Solid State Ion.* **2002**, *148*, 45.

[63] K. Nagao, A. Sakuda, W. Nakamura, A. Hayashi, M. Tatsumisago, *ACS Appl. Energy Mater.* **2019**, *2*, 1594.

[64] K. Nagao, Y. Nagata, A. Sakuda, A. Hayashi, M. Deguchi, C. Hotehama, H. Tsukasaki, S. Mori, Y. Orikasa, K. Yamamoto, Y. Uchimoto, M. Tatsumisago, *Sci Adv* **2020**, *6*, eaax7236.

[65] C. Ho, I. D. Raistrick, R. A. Huggins, *J. Electrochem. Soc.* **1980**, *127*, 343.

[66] L. Hyobin, Y. Seungwon, K. Suhwan, S. Jihun, P. Joonam, D. Chil-Hoon, H. Yoon-Cheol, K. Tae-Soon, Y. M. Lee, *Curr. Opin. Electrochem.* **2022**, *34*, 100986.

[67] S. Ohno, C. Rosenbach, G. F. Dewald, J. Janek, W. G. Zeier, *Adv. Funct. Mater.* **2021**, *31*, 2010620.

[68] W. Zhang, D. A. Weber, H. Weigand, T. Arlt, I. Manke, D. Schröder, R. Koerver, T. Leichtweiss, P. Hartmann, W. G. Zeier, J. Janek, *ACS Appl. Mater. Interfaces* **2017**, *9*, 17835.

[69] R. Koerver, I. Aygün, T. Leichtweiß, C. Dietrich, W. Zhang, J. O. Binder, P. Hartmann, W. G. Zeier, J. Janek, *Chem. Mater.* **2017**, *29*, 5574.

[70] C. Y. Kwok, S. Xu, I. Kochetkov, L. Zhou, L. F. Nazar, *Energy Environ. Sci.* **2023**, *16*, 610.

[71] F. Han, Y. Zhu, X. He, Y. Mo, C. Wang, *Adv. Energy Mater.* **2016**, *6*, 1501590.

[72] Y. Fujita, K. Motohashi, A. Sakuda, A. Hayashi, *J. Phys. Chem. C Nanomater. Interfaces* **2024**, *128*, 20774.

[73] S. Samanta, S. Bera, R. K. Biswas, S. Mondal, L. Mandal, A. Banerjee, *ACS Energy Lett.* **2024**, *9*, 3683.

[74] J. S. Kim, S. Jung, H. Kwak, Y. Han, S. Kim, J. Lim, Y. M. Lee, Y. S. Jung, *Energy Storage Mater.* **2023**, *55*, 193.

[75] T. Koç, F. Marchini, G. Rousse, R. Dugas, J.-M. Tarascon, *ACS Appl. Energy Mater.* **2021**, *4*, 13575.

[76] C. Rosenbach, F. Walther, J. Ruhl, M. Hartmann, T. A. Hendriks, S. Ohno, J. Janek, W. Zeier, *Adv. Energy Mater.* **2022**, *13*, 2203673.

[77] S. Yanagihara, J. Huebner, Z. Huang, A. Inoishi, H. Akamatsu, K. Hayashi, S. Ohno, *Chem. Mater.* **2024**, *37*, 109.

[78] A. Sakuda, A. Hayashi, M. Tatsumisago, *Sci. Rep.* **2013**, *3*, 2261.

[79] J. Zhang, C. Zheng, L. Li, Y. Xia, H. Huang, Y. Gan, C. Liang, X. He, X. Tao, W. Zhang, *Adv. Energy Mater.* **2020**, *10*, 1903311.

[80] M. Suyama, A. Kato, A. Sakuda, A. Hayashi, M. Tatsumisago, *Electrochim. Acta* **2018**, *286*, 158.

[81] E. Rangasamy, Z. Liu, M. Gobet, K. Pilar, G. Sahu, W. Zhou, H. Wu, S. Greenbaum, C. Liang, *J. Am. Chem. Soc.* **2015**, *137*, 1384.

[82] F. Han, J. Yue, X. Zhu, C. Wang, *Adv. Energy Mater.* **2018**, *8*, 1703644.

[83] M. Liu, C. Wang, C. Zhao, E. van der Maas, K. Lin, V. A. Arszelewska, B. Li, S. Ganapathy, M. Wagemaker, *Nat. Commun.* **2023**, *14*, 2370.

[84] Y. Fujita, Y. Kawasaki, T. Inaoka, T. Kimura, A. Sakuda, M. Tatsumisago, A. Hayashi, *Electrochemistry* **2021**, *89*, 334.